Proton-proton spin correlation measurements at 200 MeV with an internal target in a storage ring

W. Haeberli, B. Lorentz, F. Rathmann, M. A. Ross, and T. Wise
Department of Physics, University of Wisconsin-Madison, Madison, Wisconsin 53706

W. A. Dezarn, J. Doskow, J. G. Hardie, H. O. Meyer, R. E. Pollock, B. von Przewoski, T. Rinckel, and F. Sperisen
Indiana University and Indiana University Cyclotron Facility, Bloomington, Indiana 47408

P. V. Pancella
Western Michigan University, Kalamazoo, Michigan 49008
(Received 17 September 1996)

Measurements of the pp spin correlation coefficients A_{xx}, A_{yy}, and A_{xz} and analyzing power A_y for pp elastic scattering at 197.8 MeV over the angular range 4.5°–17.5° have been carried out. The statistical accuracy is approximately ± 0.01 for A_{mn} and ± 0.004 for A_y, while the corresponding scale factor uncertainties are 2.4% and 1.3%, respectively. The experiment makes use of a polarized hydrogen gas target internal to a proton storage ring (IUCF Cooler) and a circulating beam of polarized protons. The target polarization ($Q=0.79$) is switched in sign and in direction (x,y,z) every 2 s by reversing a weak guide field (about 0.3 mT). The forward-scattered protons are detected in two sets of wire chambers and a scintillator, while recoil protons are detected in coincidence with the forward protons by silicon strip detectors placed 5 cm from the proton beam. The background rate from scattering by the walls of the target cell is (0.2 ± 0.2)% of the good event rate. Analysis methods and comparisons with pp potential models and pp partial wave analyses are described. [S0556-2813(97)02402-3]

PACS number(s): 13.75.Cs, 25.40.Cm, 24.70.+s, 29.25.Pj

I. INTRODUCTION

The purpose of the present paper is to describe the first use of an internal polarized hydrogen gas target in a proton storage ring to measure spin correlation parameters and to report values of A_{xx}, A_{yy}, and A_{xz} at 197.8 MeV proton energy as a function of angle between $\theta_{\mathrm{lab}}=4.5°$ and 17.5°.

Physics with polarized gas targets internal to storage rings is still in the beginning phase. Early experiments with deuterium targets in electron storage rings were carried out at Novosibirsk [1,2]. A first measurement of p-^{3}He spin correlation with a $^3\vec{\mathrm{He}}$ target [3] in the IUCF proton storage ring, or ''Cooler,'' and a feasibility test with a $\vec{\mathrm{H}}$ target in the low-energy test storage ring in Heidelberg [4] are the only prior uses of internal polarized targets in proton storage rings. In all of these cases, the polarized atoms were injected into an open-ended target cell (''storage cell''; see [5]) in order to obtain a useful target thickness. Compared to ^{3}He, a polarized hydrogen target is more difficult because the production rate of polarized H by the atomic-beam method is considerably less than the production rate of ^{3}He by optical pumping. Therefore, a smaller aperture was required for the hydrogen target to compensate for the lower production rate. A small-aperture cell leads to additional constraints for the beam injection process, to a reduced machine acceptance (and thus beam lifetime), and raises concern about background from interactions with the cell walls. In addition, depolarization by collisions with the cell wall is *a priori* much more likely for the proton in a H atom than for the ^{3}He nucleus, because the proton in H can be depolarized via the hyperfine interaction if the electron depolarizes on the wall.

For the present experiment, a bombarding energy near 200 MeV was chosen because no previous pp spin correlation measurements whatever have been reported between 150 MeV and 300 MeV [6,7]. The goal of the present experiment was to develop methods that would allow a measurement of spin correlation parameters to an overall accuracy of ± 0.02 or better for laboratory angles down to about 4°. Materials used in conventional polarized targets, such as NH_3 or butanol (C_4H_9OH), contain a large fraction of material other than H, which in most cases prevents measurements at small angles. Thus, even above 300 MeV, measurements are generally limited to laboratory angles greater than 30°. However, in one case, pp scattering at laboratory angles as small as 2.5° has been studied by detecting protons scattered from a thin solid polarized target, using a magnetic spectrometer of very high resolution [8].

A 197.8 MeV polarized proton beam for injection into the Cooler was provided by the IUCF cyclotron. This injection energy was chosen to avoid the need for acceleration of the stored proton beam in the presence of the restrictive aperture of the storage cell target, since this would have required additional development work. Only recently has acceleration of the beam in the presence of the target cell been accomplished in connection with additional measurements of spin correlation parameters as a function of proton energy up to 450 MeV [9].

Since this is the first application of a hydrogen gas target to a spin correlation experiment, a significant fraction of the paper is devoted to a description of the experimental methods that were developed. Section II presents an overview of the experimental arrangement. In Sec. III we present the method used to identify pp events from an extended gas

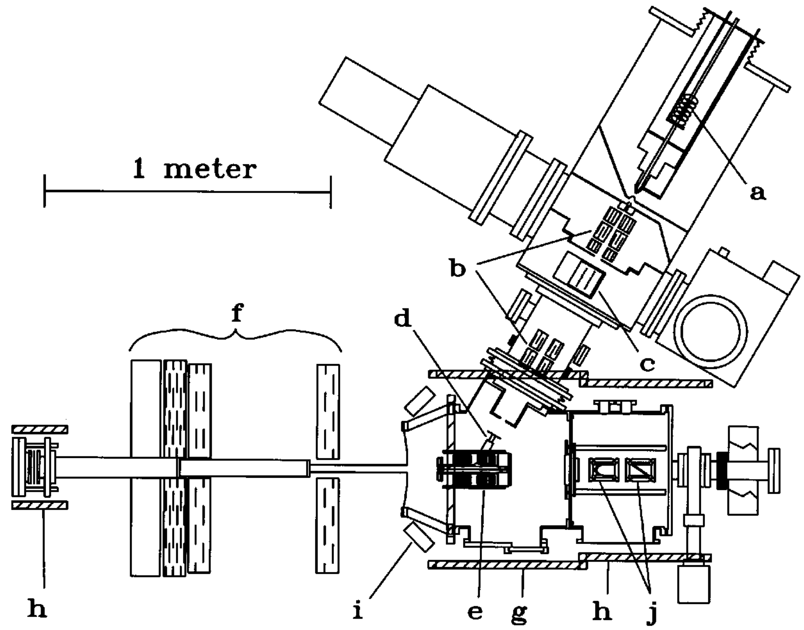

FIG. 1. Top view of the target and detector arrangement. The atomic-beam source consists of a dissociator with a cooled nozzle (a), a set of spin-separation sixpole magnets (b), and an rf transition unit (c) which is needed to select a single hyperfine state. The atoms are injected into the target cell through the feed tube (d). Silicon strip recoil detectors (e) are in coincidence with the forward detector (f). The coils (g), which provide a weak guide field over the target, are combined with compensating coils (h) which reduce the effect of the guide field on the proton closed orbit. Four scintillators (i) detect protons near $\theta_{lab}=45°$. Beam position monitors (j) are placed upstream of the target.

target, and Sec. IV discusses the methods used to determine beam position and beam motion with respect to the detectors. The results on the properties of the polarized gas target (target polarization, target thickness) are reported in Secs. V and VII. The method of measuring and reversing the polarization of the stored beam is summarized in Sec. VI. Extraction of spin correlation parameters from the measured yields and a comparison of the results to pp phase parameters are the subjects of Secs. VIII and X. Estimates of systematic errors are given in Sec. IX, followed by an outlook for applications of the new technique (Sec. XI).

Here we report only the results of the most recent 1-week run, in which about 4×10^6 elastic pp events were observed. This measurement was preceded by several runs in which the techniques presented here were developed. While we do not report comparison of the final data with the preliminary measurements, it is important to point out that exploratory results obtained under adverse conditions were in good agreement with the final results.

II. EXPERIMENTAL ARRANGEMENT

A. Overview

The major components of the target and detectors are shown in Fig. 1. The arrangement consists of an atomic-beam source which injects polarized H atoms into a target cell with thin Teflon walls. Scattered protons are detected by a forward detector, which operates in coincidence with recoil detectors surrounding the target cell. In addition, scattered protons near 45° in the laboratory system were detected by four scintillators placed 90° apart in azimuthal angle ϕ. The 45° detectors served as a convenient on-line monitor of beam and target polarization.

B. Source of polarized atoms

The atomic-beam source, which has been described in Ref. [10], selects atoms in a single hyperfine state (state 1, $m_j=+1/2$, $m_I=+1/2$; see Ref. [11]) in order to achieve high target polarization in a weak magnetic field. Measurements of the atomic beam intensity prior to installation of the source in the IUCF Cooler indicated that 3.1×10^{16} polarized hydrogen atoms/s enter the 10 mm diameter entrance tube of the storage cell. For technical simplicity the target cell is operated near room temperature, even though it is well established [12,4] that the target thickness can be increased without loss of polarization by cooling the cell wall as low as 100 K. In the present application, a weak guide field (on the order of 0.3 mT) over the target is used. A weak field has the advantage that the direction and sign of the target polarization can readily be changed by switching the current in coils exterior to the target vacuum chamber. A field that is strong compared to the critical field of the hyperfine interaction in H (50.7 mT) would have the advantage that it permits the use of two spin states (see Ref. [11]) with a corresponding increase in target density, but such strong a field would cause

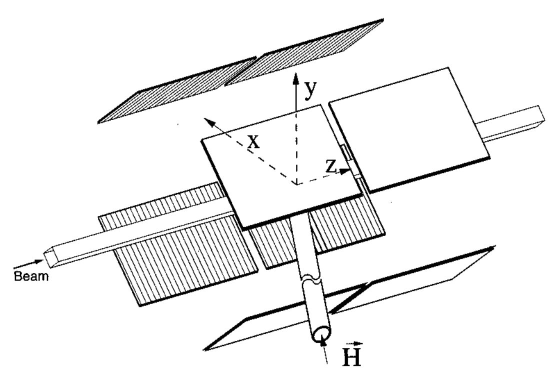

FIG. 2. View of target cell and silicon-strip recoil detectors. The target cell is 254 mm long and has an aperture for the proton beam of 8 mm × 8 mm. The 4 cm × 6 cm recoil detectors have 28 strips each of width 2.18 mm. The origin of the coordinate system is at the center of the target cell. The beam polarization is along the vertical $\pm y$ axis. The target polarization is alternating between $\pm x$, $\pm y$, and $\pm z$. The entrance tube for the H atoms is in the (horizontal) x-z plane.

large perturbations of the proton closed orbit, and in addition the magnets necessary to provide the field would impede a free view of the target by the detectors.

C. Target cell

A target cell (''storage cell'') is used because the target thickness from a jet of polarized atoms is not sufficient to provide a reasonable count rate. The present target cell, shown schematically in Fig. 2, has an 8 mm × 8 mm square cross section and a length of 25.4 cm. Polarized atoms are injected through a feed tube of diameter 10 mm and length 13 cm. The feed tube makes an angle of 60° to the proton beam to avoid interference of the atomic-beam apparatus with the detectors at forward angles. In the present case, the use of a target cell increases the target thickness over that of a jet target by a factor of about 100. The main disadvantage of a target cell over a jet target is that the cell aperture restricts the ring acceptance.

The proper choice of cell aperture is important. It can be shown [13] that the time-averaged luminosity λ is roughly proportional to $\tau \cdot d_t \cdot f_r$, where τ is the beam lifetime, d_t the target thickness, and f_r the orbit frequency. A small cell aperture increases d_t but reduces τ and vice versa, so that λ has a maximum for some value of d_t, i.e., for a certain cell aperture. The present choice of target aperture was based on measurements of λ for four different cell openings reported in Ref. [14]. Choosing a target aperture slightly larger than that for optimum λ reduces possible background from interaction of the beam with the cell walls with little loss in luminosity.

Inherent in the use of a storage cell target is the possibility of depolarization of the H atoms in wall collisions. Studies of wall depolarization as a function of wall temperature for many different wall materials and wall coatings have been reported in Ref. [12]. Aluminum walls coated with Teflon were found to have excellent polarization retention from room temperature down to 100 K [15]. For the present measurements, a very thin wall was needed for low-energy recoils to be detected, resulting in the choice of a 0.43 mg/cm^2 self-supporting Teflon foil as wall material. The energy loss in the foil for the 970 keV recoils associated with the smallest forward-scattering angle is less than 100 keV. The construction of the target cell and preparation of the thin Teflon foils are described in Refs. [16,17].

D. Target guide field

The determination of spin correlation parameters requires different orientations of the target polarization with respect to beam momentum and beam polarization. An external field was applied along either the $\pm x$, $\pm y$, or $\pm z$ direction (see Fig. 2 for coordinate system) by coils external to the vacuum chamber. Compensation coils were added immediately before the target (Fig. 1) and 2 m downstream of the target to reduce the effect of the guide field on the proton closed orbit. The guide field varied by about 30% in magnitude (but not in direction) along the central 12 cm of the target. Test measurements were made with different guide fields between ± 0.1 mT and ± 2 mT. For too low a guide field, ambient fields cause a decrease in the target polarization averaged over the active length of the target. On the other hand, an unnecessarily large guide field is to be avoided to reduce unwanted beam position modulations when the field is reversed. As a compromise, for the final measurements, the mean guide field over the active part of the cell (weighted by the target density) was $B_x = 0.25$ mT, $B_y = 0.33$ mT, and $B_z = 0.60$ mT. The ambient field at the center of the cell was compensated by adding appropriate offset currents to all guide field currents. Measured values of target polarization are presented in Sec. VII.

E. Recoil detectors

Recoil protons were detected by eight silicon strip detectors of dimension 4 cm × 6 cm each, placed 50 mm from the beam axis (Fig. 2). The detectors are positioned at azimuthal angles of $\phi = \pm 45°$ and $\pm 135°$ to permit clearance between the detectors for the atomic-beam entrance tube, which is in the horizontal plane. It can be shown in general that for given beam and target polarization directions the information content of the measurements is invariant against rotation of the detector assembly about the z axis. For example, the 45° rotation in ϕ employed here reduces the left-right asymmetry which results from the vector polarization of beam or target by a factor of $\sqrt{2}$ compared to an arrangement with detectors in the horizontal and vertical planes, but the number of counts in the left or right detector pair is doubled, thus yielding identical statistical errors.

The recoil detectors were nominally 1 mm thick, totally depleted silicon strip detectors [18]. In practice, complete depletion was rarely achieved because the applied voltage was limited by breakdown. The performance was improved somewhat by using the first and last strips of each detector as a guard ring and by cooling the entire target assembly to about 0 °C. Each detector had 26 active strips along the beam direction to provide information about the z coordinate of the interaction. The detectors cover only about half of the length of the target. The part of the target viewed still corresponds to roughly 3/4 of the total target thickness because the target density drops linearly from a maximum at the cell center, where the feed tube enters, to practically zero at either end.

F. Forward detector

The forward-scattered protons exit the scattering chamber through a stainless steel window of 0.13 mm thickness, while protons scattered near 45° exit through the 1 mm thick conical part of the chamber (Fig. 1). The rms multiple scattering angle in the two cases is 0.2° and 1.3°, respectively.

The forward detector consists of two planes of wire chambers [19] (wire spacing 6.35 mm) and a plastic scintillator segmented into eight elements. An aluminum plate 7.6 cm thick was placed in front of the 10 cm thick scintillator in order to stop the protons in the scintillator. For a detailed description of the forward detector see Ref. [20].

III. DATA ACQUISITION AND PROCESSING

A. Measuring cycle and data recorded

The beam is injected from the cyclotron into the Cooler for a given length of time (e.g., 300 s) or until a predeter-

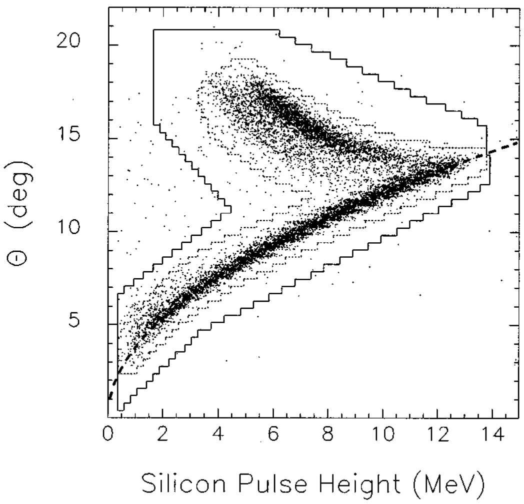

FIG. 3. Energy loss E_r in a recoil detector vs forward scattering angle θ determined by the wire chambers. The solid and dotted lines indicate the areas of accepted events for wide and narrow cuts, respectively. The dashed line shows the predicted relationship between θ and E_r, based on the detector energy calibration with α particles (Fig. 4).

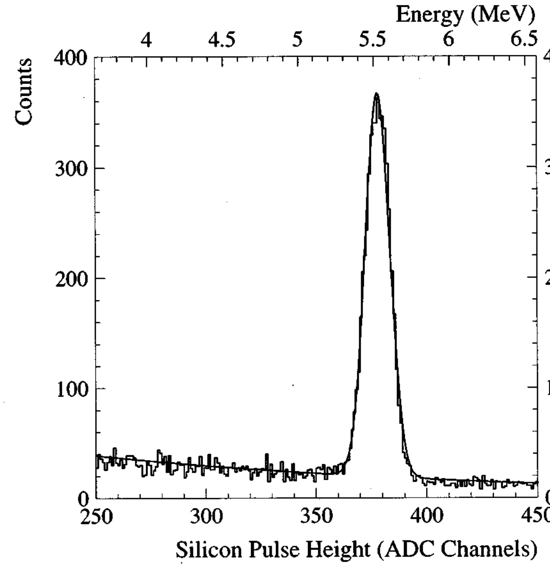

FIG. 4. Pulse height spectrum of a silicon strip recoil detector in the presence of a proton beam though the polarized H target. The peak is caused by α particles from a 10-Hz ^{241}Am source permanently mounted near the detector. The counts away from the α peak are from pp scattering and background. The spectrum illustrates the low singles rate in a dector near the circulating beam. The curve is a Gaussian of width 80 keV, superimposed upon an exponential background.

mined beam intensity has accumulated. Injection is followed by a 765 s measuring cycle when the beam is available to the experiment.

The first and last few seconds of the measuring cycle are used to turn the wire chambers and target gas on and off. The remaining time is organized into 60 subcycles of 12 s each, during which the target polarization direction is changed every 2 s (see Sec. II D). A spin flipper (Sec. VI) reverses the polarization of the stored proton beam after 10 subcycles and again after an additional 30 subcycles. At the end of a cycle, data acquisition was stopped, the Cooler magnets were reset, and additional beam was accumulated in the ring.

The recording of an event was triggered by either one of two conditions. The first type of event was a coincidence between the forward scintillator and any of the silicon recoil detectors. The second type of event is a coincidence between either of the two upper and either of the two lower 45° detectors. The second signature included the opposite pairs that are triggered by pp elastic scattering as well as adjacent pairs that can only occur with background $(p,2p)$ reactions.

The event record for both types of triggers contained the energy and the time with respect to the occurrence of the trigger of all scintillators and silicon detectors. In addition, signals that provide the silicon strip position information, as well as the number of any of the 448 wires in the four wire chamber planes, were recorded. Also stored with each event was the time of occurrence with respect to the cycle start and with respect to the beginning of the current target polarization subcycle, as well as a number of dc levels, for the current in the guide field coils and logic levels signaling the sign of the beam polarization as well as the sign and direction of the target polarization.

The singles rates of all detectors, some coincidence rates, and a rate from a frequency-converted beam-current monitor were sent to scalers. The content of these scalers was read once a second, a rate was calculated, and displayed as a function of the time from the start of a cycle. This information was used, for instance, to determine the dead time of the data acquisition system.

B. Conditions on accepted events

1. Recoil energy

The correlation between energy loss in the recoil detectors and forward angle θ determined from the wire chambers is shown in Fig. 3. For $\theta < 13°$ the recoil protons stop in the detector, while for larger angles they pass through the detector. The large spread in pulse height for protons passing through the detector is the result of incomplete depletion of the detector and variation of the resistivity of the detector over its area.

For protons that stop in the detector the recoil pulse height can be predicted provided the absolute energy calibration of each recoil detector is known. The calibration is provided by ^{241}Am α sources which are installed permanently near each detector. Since the α particles produce no coincidences, the calibration required the recording of events (''singles'') which were only registered in the silicon detectors. An example of such a spectrum taken in the presence of beam through the H target is shown in Fig. 4. The detector gain calibration is reproducible to 0.5% and shows no measurable dependence on magnetic guide field or on count rate. It is interesting to note that the singles rate in the recoil detectors is quite low in spite of the presence of the beam in the target cell. The 10 Hz rate of α-pulses is more than a factor 10 greater than the rate of pp events and background with the same deposited energy (Fig. 4). Thus the fear that the circulating beam only 5 cm away from the silicon detectors would produce a large background turned out to be unfounded,

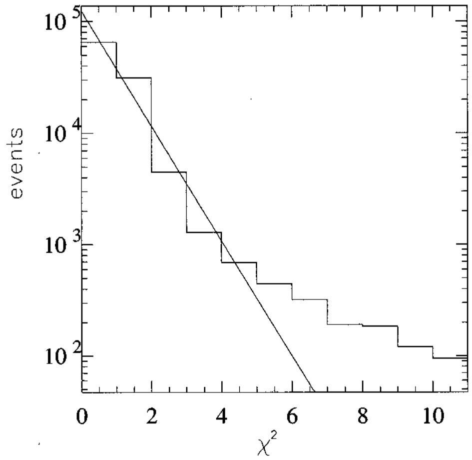

FIG. 5. Distribution of χ^2 for a sample of 10^5 coincident events between recoil detectors and forward detectors. The χ^2 measured the quality of agreement between five coordinates per event determined by the detectors and the three coordinates: scattering angle θ, azimuthal angle ϕ, and the z coordinate of the vertex.

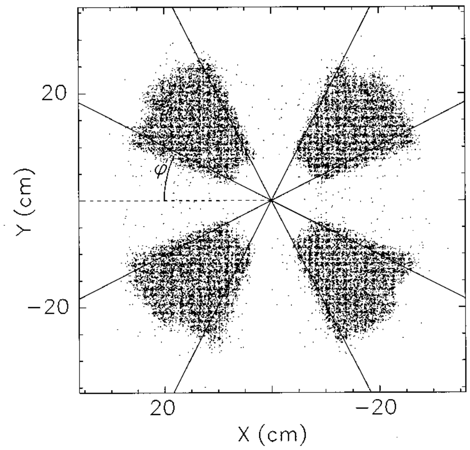

FIG. 6. Distribution of forward protons vs coordinates in the second wire chamber, as seen in the beam direction, in coincidence with the recoil detectors. The four lobes correspond to the four recoil detectors. In the data analysis, events are accepted in a ϕ interval of $\pm 18°$ about $\phi = \pm 45°$, $\pm 135°$.

even in the absence of a coincidence requirement. On the other hand, high detector rates during filling of the ring are of concern because of possible radiation damage to the recoil detectors. Radiation damage was reduced by placing a beam blocker in the straight section immediately after injection. The blocker had the purpose of attenuating protons which, during injection, enter the ring but are outside the phase space acceptance. The position of the blocker is adjusted such that, without affecting the beam lifetime, the count rate in the silicon detectors is as small as possible.

In Fig. 3, the predicted recoil pulse height vs θ is represented by the dashed curve. The calculation takes into account the energy loss in the cell wall. The excellent agreement indicates that for $\theta < 13°$ the scattering angle can be determined from the recoil pulse height alone. The rms deviation between θ determined by the forward detector and by the recoil detector pulse height is 0.2°, which is accounted for primarily by multiple scattering in the exit window of the target chamber. Below 4° the deviation increases because the forward protons pass through the inner wire support of the first wire chamber. While the scattering angle can in principle be determined from the recoil pulse height rather than the forward detector, no useful data were obtained for $\theta < 4°$ because the silicon pulse height was too small to be separated cleanly from detector noise.

For most events, the z coordinate of the vertex could be determined from the silicon position spectrum since only one strip (or two adjacent strips) fired. In cases where the position signal was ambiguous, the position was assumed to be in the center of the detector and a position uncertainty equal to half the length of the detector was assigned.

2. Identification of pp events

The first wire chamber was 50 cm from the target center, the second one 95 cm. Detection of the forward particle in the two wire chamber planes permits determination of the scattering angle θ and the azimuthal angle ϕ. If a cluster of wires (up to four adjacent wires) fired in a given wire plane, the coordinate of the track was determined from the centroid of the cluster. Clusters with more than four wires were ignored. The analysis of each event made use of up to five coordinates (four wire chamber coordinates and the z position of the silicon strip that fired) to determine three parameters θ, ϕ, and the z coordinate of the vertex by a least-squares fit. An example of a typical χ^2 distribution for events which satisfy the recoil pulse height criterion (wide cut in Fig. 3) is shown in Fig. 5. The expected distribution for two degrees of freedom is an exponential. In calculating χ^2, the assumed variance in wire chamber coordinates was 3 mm, i.e., half the wire spacing. The slope of the straight line in

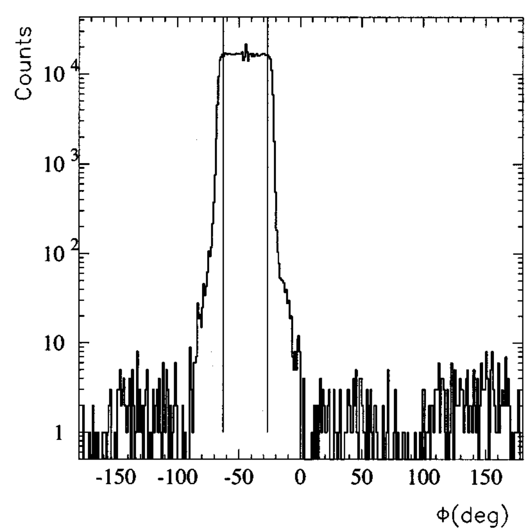

FIG. 7. Number of counts vs ϕ for pulses in coincidence with one recoil detector. The events shown are selected to be inside the wide gate of Fig. 3 and to satisfy the criterion $\chi^2 > 6$ for the forward track. The small fraction of counts outside the ϕ interval defined by the detector illustrates the absence of noncoplanar events from background such as $(p,2p)$ reactions in the cell wall.

Fig. 5 is steeper than expected. The measured slope indicates that the actual uncertainty with which a wire chamber determines a track position is ± 2.0 mm.

Events in the range $3 < \chi^2 < 20$ were found to give final results for A_{mn} that are statistically consistent with the events with $\chi^2 < 3$. In the final analysis, events with $\chi^2 < 6$ ($\sim$98% of all events) were accepted.

For about 10% of events there was more than one cluster of wires that fired in one of the wire chambers. After evaluating all possibilities, the track with the smallest χ^2 was accepted. The same applies to events when more than one silicon detector fired.

Figure 6 shows the hit pattern of protons in the second wire chamber in coincidence with the recoil detectors, and Fig. 7 shows the number of counts vs ϕ for a single recoil detector. For Figs. 6 and 7 the range in ϕ is given by the size of the recoil detectors. To be considered a valid pp event a condition is imposed that the recoil and forward tracks are on opposite sides, and that the azimuth is in a $\pm 18°$ interval with respect to the central values $\phi = \pm 45°$, $\pm 135°$. Thus the software cut and not the boundaries of the recoil detectors determines the ϕ range.

IV. DETECTOR GEOMETRY WITH RESPECT TO THE BEAM

Because the pp events are overdetermined, the data themselves can be used to find the positions of the detectors very precisely. The distance between the two wire chambers can be measured directly, but the distance to the center of the target cell in the vacuum chamber (and thus to the recoil detectors) is determined in the following way: All of the proton tracks measured by the wire chambers in a given run are projected back onto an xy plane at the z coordinate of each vertex, as determined by the recoil detectors. An example of the resulting pattern is shown in Fig. 8. The calculation is repeated for different assumed distances between wire chambers and target center. The distance that produces the smallest spread in the hit pattern then yields the target position relative to the wire chambers to ± 0.7 mm.

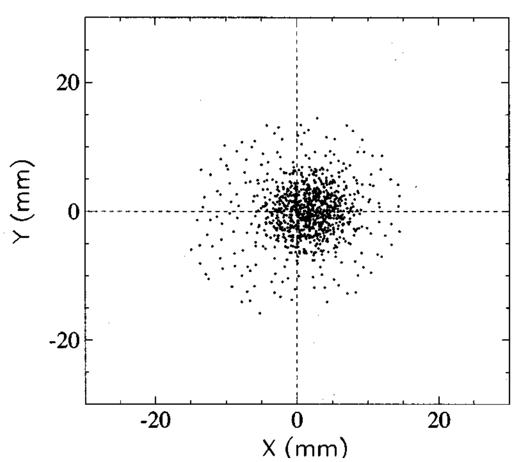

FIG. 8. Hit pattern in the plane perpendicular to the vertex. Based on the positions in the two wire chamber planes, each track is projected back onto an x-y plane at the location z determined from the z position of the recoil strip and from the scattering angle θ. The spread in the hit pattern reflects the finite resolution of the wire chambers rather than the beam size.

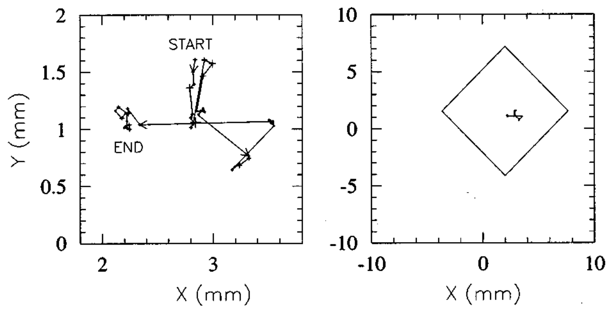

FIG. 9. Beam motion during a 1-week run. Each dot corresponds to the average beam position during a run of typically 2 h duration. Note that the changes in beam position are small compared to the 8-mm cell aperture. The relatively large changes (1 mm) in beam position are associated with retuning the accelerator after a power failure or other major changes in beam tuning. In the right-hand figure, the position of the cell walls relative to the beam is indicated.

Hit patterns, like the one shown in Fig. 8, were used to detect misalignment of the beam relative to the wire chambers. This misalignment is removed by a corresponding software adjustment of the transverse wire chamber position. Figure 9 shows that the misalignment varies with time as a result of drifts in beam position. The statistical error in the position of the centroid of the hit pattern for each run is about ± 0.1 mm. Note that the beam motion (Fig. 9) during a 1 week run is small compared to the 8 mm cell aperture. The largest change in beam position is of the order 1 mm and is associated with retuning the accelerators after a power failure.

Shifts in beam angle with respect to the symmetry axis of the wire chambers were also determined off line. For a given track, the scattering angle can be determined either from the wire chamber coordinates or from the pulse height in the recoil detectors, provided the recoils stop in the detectors. An angular offset of the beam with respect to the wire chambers reflects itself in a disparity between these two angle measures. By analyzing a large number of events and exploiting the redundancy arising from multiple recoil detectors, the beam angle offset could be determined to an accuracy of $\pm 0.05°$, including estimated systematic errors.

At the beginning of a running period, the beam was centered with respect to the cell by measuring the beam lifetime as a function of beam position, using deflectors in the ring to displace the beam. In order to increase the sensitivity of the beam lifetime to beam position, N_2 was added in another part of the ring to increase beam heating. By recording the beam lifetime vs beam displacement the center of the cell was established. The position of the cell wall shown in Fig. 9 is based on such measurements. Since the cell has no remote position adjustment, the available range of deflection was not always sufficient to reach the center of the cell. The position of the cell wall with respect to the beam is subject to about 1 mm uncertainty, which, however, is of no consequence for the measurements.

V. BEAM CURRENT, TARGET THICKNESS, LUMINOSITY, AND COUNT RATE

The proton beam was accelerated in the IUCF cyclotron, extracted, and kick-injected into the Cooler. The accumulation rate of injected and stored beams was in the range 10–30 μA/min. At the end of the cycle, additional beam was injected to add to the already existing beam in the ring, leading to stored beam currents of up to 300 μA. The beam lifetime was typically 20–30 min, depending on vacuum conditions and tuning of the ring. However, under given conditions, the beam lifetime was independent of the presence of polarized H in the target.

The thickness of the polarized target was determined by comparing the pp count rate with that for an unpolarized H_2 target whose thickness was known from the H_2 flow rate into the center of the cell and the gas conductance of the cell. The result, $d_t = 3.1\times 10^{13}$ H/cm^2, is in good agreement with the thickness expected from absolute measurements of the atomic-beam flux prior to installation of the target of $d_t = (3.5\pm 0.3)\times 10^{13}$ H/cm^2. The target thickness varied less than 10% during the 1 week run. The part of the target viewed by the detectors has a thickness of about 2.2×10^{13} H/cm^2.

One would expect the target thickness to be invariant under changes in sign and direction of target polarization. The relative target thickness is measured accurately by comparing the total number of counts in all detectors, summed over both beam spin states. Earlier runs showed up to a 20% variation of target thickness when the guide field in the x direction was reversed. The reason was that the stray field from the guide field coils affected the field in the rf transition unit which rejects one of the hyperfine states in the atomic-beam source. The stray field changed the transition probability and thus the target density as well as the magnitude of the target polarization. After the addition of a compensation coil prior to the final measurements, no variation in target thickness was detectable at the level of 0.3%. This implies that within this accuracy the efficiency of the rf transition is independent of guide field. For an unpolarized target, changes in direction and sign of the guide field had no measurable effect.

The observed number of pp events normalized to the integrated proton charge passing through the target is about 6×10^4 counts/C. Under best conditions, 10^6 pp elastic scattering events were accumulated in 1 day. This corresponds to an average luminosity of 2.5×10^{28} s^{-1} cm^{-2}.

VI. BEAM POLARIZATION AND SPIN FLIPPER

Polarized protons were produced by an atomic-beam-polarized ion source [21]. Rather than changing the sign of polarization at the ion source by switching between two different rf transition units, a spin flipper was used to reverse the spin of the stored beam. The principal advantage of the spin flipper is that the average luminosity of the experiment is increased since rather than discarding the beam at the end of a cycle additional particles of the same spin direction are added to the beam remaining in the ring. The spin flipper principle had been tested previously at IUCF by Caussyn *et al.* [22], but had not been used for data acquisition. A high reliability of the flipper is important, because if one flip is missed the experiment falls out of step. Recovery of the information would still be possible off line, since there is enough statistical accuracy between flips to confirm that the sign of polarization has reversed, but would be tedious. For each cycle the beam polarization was flipped twice, timed in such a way that about the same luminosity for spin up and spin down was obtained (Sec. III A). About 500 sign changes were carried out in a 1-week run; all were successful. The flipping efficiency was (97.1 ± 0.3)%. The slight loss in beam polarization for each flip is more than offset by the large increase in average luminosity. The operation of the flipper is described in more detail in Ref. [23].

The beam polarization was continuously monitored as part of the spin correlation measurements. The determination of beam and target polarization in terms of the detector yields is discussed in Sec. VIII. As described in more detail below (see Sec. VIII D), the calibration of beam and target polarization is based on a previous absolute calibration of the analyzing power in pp scattering at 183.1 MeV [24]. Under normal running conditions, the beam polarization measured in the ring was consistent with the polarization measured in the injection beam line. However, after interruptions caused by equipment failures, the beam stored in the ring was often found to be unpolarized, the depolarization being caused by the close vicinity of an intrinsic depolarizing resonance to the present beam energy. Polarization could be restored by adjusting the tune. Once established, the polarization remained constant within statistics (about 0.03) from run to run.

In order to determine the spin correlation coefficients, the average of the product of beam and target polarization $\langle PQ\rangle$ is required. This is different from the product of the measured $\langle P\rangle$ and $\langle Q\rangle$, if both quantities change significantly with time. For the present measurements, target and beam polarizations were sufficiently constant to be able to sum counts for all runs in the analysis.

Beam polarizations were evaluated separately for the three different directions of magnetic guide field over the target. The results indicate that the guide field has no effect

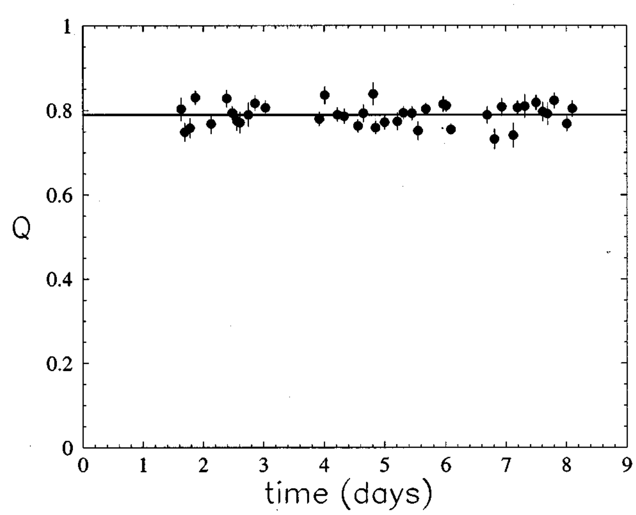

FIG. 10. Variation of target polarization during the most recent 1-week run. Gaps are caused by accelerator failures. The values shown are $Q = 1/2(Q_x + Q_y)$.

TABLE I. Summary of target polarization for different guide field directions. The results are averages of measurements taken during a 1-week run. The uncertainties are statistical and do not include the absolute polarization calibration error of about 1.3%. As a check, the measurement was also carried out with unpolarized H_2 in the target cell.

		Guide field direction		
Target	Target pol.	B_x	B_y	B_z
$\vec{H}$	Q_x	0.785 ± 0.005	0.008 ± 0.005	0.006 ± 0.005
$\vec{H}$	Q_y	-0.006 ± 0.005	0.796 ± 0.005	-0.008 ± 0.005
H_2	Q_x	-0.003 ± 0.006	-0.005 ± 0.006	0.000 ± 0.006
H_2	Q_y	0.002 ± 0.006	-0.002 ± 0.006	-0.003 ± 0.006

on either the magnitude or direction of the beam polarization. From experiments in which for the last part of each cycle unpolarized H_2 gas was injected into the target cell rather than polarized H, it was determined that the presence of target polarization has no effect on beam polarization. It has been predicted [25] and observed [26] that passage of the beam through a polarized target causes a slow change in beam polarization, but these effects are too small to be relevant in the present experiment.

VII. TARGET POLARIZATION

The degree of polarization in the x and y directions (Q_x, Q_y) is determined from the asymmetry in count rate associated with reversal of the target polarization (see Sec. VIII). No deterioration of target polarization (radiation damage to the cell walls) was observed during the recent 1-week run (Fig. 10) nor in any of the previous runs. Table I shows that the target polarization is equal in magnitude independent of the guide field direction ($Q_x=Q_y$) and that the polarization component orthogonal to the desired direction is small. Without the availability of longitudinal beam polarization the longitudinal target polarization (Q_z) cannot be measured directly. In the analysis, Q_z is taken as the average of Q_x and Q_y.

It is important to test if spurious effects might be introduced by reversal of the guide field, such as effects caused by small changes in beam position or beam angle. Results obtained with an (unpolarized) H_2 target, which were alternated with the polarized-target measurements, are also shown in Table I. For all guide fields, the results are consistent with zero.

The uncertainties in target polarizations in Table I do not include a 1.3% absolute calibration uncertainty (see Sec. VIII D). Even if this added uncertainty is taken into account, the target polarization is significantly lower than the value of $Q=0.87$ expected from the calculated spin-rejection factors of the atomic-beam source and the measured transition probability of the rf transition unit [16]. Since the target polarization is monitored continuously, the difference is of no consequence to the actual measurement. A possible explanation for the roughly 10% shortfall in target polarization could be depolarization of H atoms in wall collisions, in which case the target polarization would show a dependence on z, since the target atoms near the center of the target have in the average suffered fewer wall collisions than those that have diffused away from the center of the cell. The z dependence of the target polarization, deduced from pp scattering events originating at different z positions, is shown in Fig. 11. No z dependence in Q is observed. The results indicate that the

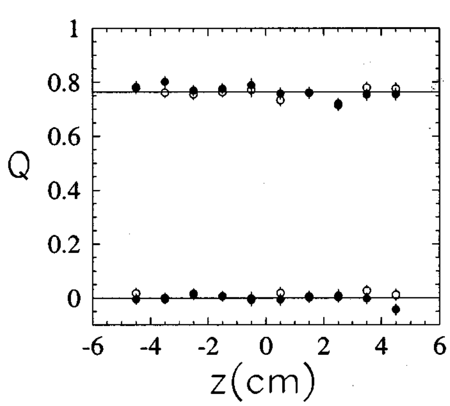

FIG. 11. Target polarization Q as a function of position along the target cell. The atomic beam enters the cell at $z=0$. The open circles refer to Q_x, the solid dots to Q_y. The components of Q_x, Q_y transverse to the intended target polarization directions are also shown.

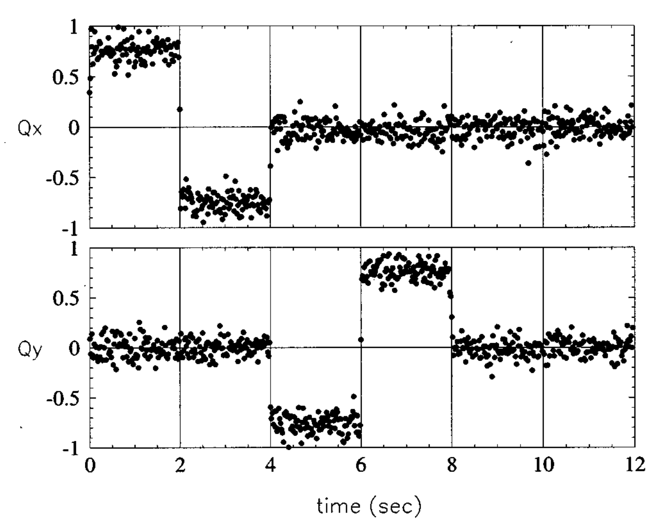

FIG. 12. Target polarization components Q_x and Q_y as a function of time over a 12-s cycle. The results are based on left-right and up-down count rate ratios measured with the polarized H target relative to the corresponding ratios measured with H_2 in the target cell. From $t=8.0$ to 12.0 the target is polarized in the z direction.

depolarization probability per wall collision is less than 2×10^{-4}. It is interesting to note that in the earlier test of polarized H target cells in the storage ring in Heidelberg [4], the same 10% discrepancy between expected and measured polarization was observed.

The target polarization was reversed every 2 s and was cycled between Q_x, Q_y, and Q_z in a 12-s subcycle. The rise time of the target polarization was measured by binning the counts in 20-ms bins and calculating the polarization for each bin. Figure 12 shows that the polarization rise time is less than 50 ms. The rise time of the guide field is limited by eddy currents induced in the walls of the scattering chamber and in the aluminum frames on which the guide field coils are wound. To assure that the target polarization has reached the full value, the first 100 ms of data after a change in the guide field are rejected.

VIII. DETERMINATION OF SPIN CORRELATION COEFFICIENTS

A. Definitions and description of the problem

The differential cross section σ for a polarized beam on a polarized target in units of the unpolarized cross section σ_0 is given by

$$\sigma/\sigma_0=1+[(p_y+q_y)\cos\phi-(p_x+q_x)\sin\phi]A_y+[(p_xq_z+p_zq_x)\cos\phi+(p_yq_z+p_zq_y)\sin\phi]A_{xz}$$
$$+(p_xq_x+p_yq_y)(\cos^2\phi A_{xx}+\sin^2\phi A_{yy})+(p_xq_y+p_yq_x)\sin\phi\cos\phi(A_{xx}-A_{yy})+p_zq_zA_{zz}\,. \tag{1}$$

Here, $p_{x,y,z}$ and $q_{x,y,z}$ are the components of the polarization vector for beam and target, respectively, in a frame where z points along the beam, y upwards and $x=y\times z$, and ϕ is the azimuthal angle as defined in Fig. 6. The analyzing power A_y and the spin correlation coefficients A_{mn} are functions of the scattering angle θ.

As explained earlier, data were obtained in sequence, with the target polarized along all three coordinate axes. For each target direction, both beam and target polarizations along $(+)$ or opposite $(-)$ to the respective coordinate axis were used, resulting in the following sequence of four polarization states: $(+,+)$, $(+,-)$, $(-,+)$, $(-,-)$, where the first sign refers to the beam, and the second to the target. We label these four states with the index $k(k=1,\ldots,4)$. For the moment, we assume that $p_y=\pm P_y$, $q_x=\pm Q_x$, etc., i.e., that sign reversal does not affect the magnitude of the polarization (denoted by capital letters). Possible small differences between $+$ and $-$ polarizations will be discussed later. Thus, each term in Eq. (1) contains the magnitude of polarization of beam (P) or target (Q) or both, and a sign factor μ. The sign factors for the four polarization states, and for terms that contain only P are $\mu_{P,k}=(+,+,-,-)$, $\mu_{Q,k}=(+,-,+,-)$ for terms with only Q, and finally, for terms that contain both P and Q, $\mu_{PQ,k}=(+,-,-,+)$.

Data were acquired in four intervals of azimuthal angle (of the forward proton). These intervals are centered at $\phi_1=(45°,-45°,-135°,135°)$ where the index i labels the respective quadrant $(i=1,\ldots,4)$, and the angle ϕ is defined in Fig. 6. Data within a range of $\phi_i\pm\Delta\phi$ are accepted. A range of $\Delta\phi=18°$ was chosen such that the associated recoils were entirely within the ϕ acceptance of the silicon detectors (solid lines in Fig. 6).

The trigonometric functions of ϕ in Eq. (1), when averaged over the ϕ acceptance $\Delta\phi$, have the same magnitude for all four ϕ_i, namely, $|\langle\sin(\phi_i)\rangle|=|\langle\cos(\phi_i)\rangle|=c_1$, $|\langle\sin^2(\phi_i)\rangle|=|\langle\cos^2(\phi_i)\rangle|=1/2$, and $|\langle\sin(\phi_i)\cos(\phi_i)\rangle|=c_2$, where $c_1=(\sqrt{2}/2)\sin(\Delta\phi)/\Delta\phi$ and $c_2=\frac{1}{2}\sin(2\Delta\phi)/2\Delta\phi$. The signs ν of these functions, however, are different for the four quadrants $(i=1,\ldots,4)$: For terms with $\sin\phi$, we obtain $\nu_{s,i}=(+,-,-,+)$, and for terms with $\cos\phi$, $\nu_{c,i}=(+,+,-,-)$, with the obvious extension to combined functions, e.g., $\nu_{s,c}=\nu_s\cdot\nu_c$. Possible small deviations of the centroid of the true ϕ acceptances from the ideal values ϕ_i will be discussed later.

Given these definitions we can now rewrite Eq. (1) to represent the differential cross section measured with a specific polarization state (index k) with the detector at a given azimuth (index i). Since only vertical beam polarization was used in this experiment, we set $P_x=P_z=0$; however, the possibility of small nonvertical components is not excluded and will be discussed below. For a sideways polarized target (only terms with Q_x enter), Eq. (1) then becomes

$$\sigma_{ik}/\sigma_0=1+[\nu_{c,i}\mu_{P,k}]c_1P_yA_y-[\nu_{s,i}\mu_{Q,k}]c_1Q_xA_y$$
$$+[\nu_{sc,i}\mu_{PQ,k}]c_2P_yQ_x(A_{xx}-A_{yy}). \tag{2}$$

Similarly, for a vertically polarized target,

$$\sigma_{ik}/\sigma_0=1+[\nu_{c,i}\mu_{P,k}]c_1P_yA_y-[\nu_{c,i}\mu_{Q,k}]c_1Q_yA_y$$
$$+[\nu_{ss,i}\mu_{PQ,k}]\frac{1}{2}P_yQ_y(A_{xx}+A_{yy}), \tag{3}$$

and, finally, with longitudinal target polarization we have

$$\sigma_{ik}/\sigma_0=1+[\nu_{c,i}\mu_{P,k}]c_1P_yA_y+[\nu_{s,i}\mu_{PQ,k}]c_1P_yQ_zA_{xz}\,. \tag{4}$$

Each of these equations represents a set of 16 combinations of polarization state k and azimuth ϕ_i. These combinations differ only in the sign factors $[\nu\cdot\mu]$ appearing in front of the polarization terms. These ''sign matrices'' are characteristic for the term with which they are associated, and using the definitions given above, it is easy to derive them. For instance,

$$[\nu_{c,i}\mu_{P,k}]=\begin{pmatrix} + & + & - & - \\ + & + & - & - \\ - & - & + & + \\ - & - & + & + \end{pmatrix}. \tag{5}$$

To explain this further, let us evaluate the cross section, measured in the quadrant centered at $\phi=45°$ (use $i=1$), with beam polarization pointing ''up'' and target polarization to the left [use Eq. (2) and $k=1$]. We find

$$\sigma_{11}/\sigma_0=1+c_1P_yA_y-c_1Q_xA_y+c_2P_yQ_x(A_{xx}-A_{yy}). \tag{6}$$

For the other three polarization states ($k=2,\ldots,4$) three more equations result, differing only by the signs. If the cross sections σ_{1k} were actually known, it is easy to see that the resulting four equations can be used to deduce the quantities P_yA_y, Q_xA_y, and $P_yQ_x(A_{xx}-A_{yy})$ by simply adding the σ_{1k} with the appropriate signs. By introducing a calibration for A_y at one angle (see Sec. VIII D), the analyzing power and the spin correlation parameters can be deduced at all angles.

So far, only one detector azimuth has been used. The same procedure can be applied to the other three detector locations. This additional information is used to determine the luminosities for the polarization components and differences in magnitude between + and − polarization, as will be shown in the following.

B. Observed yields: diagonal scaling

In this experiment we measure the yields in each of four quadrants i and each of four polarization states k, i.e., 16 numbers Y_{ik} in all. Such a set of 16 yields is obtained for each scattering angle interval $\Delta\theta$ and each of the three possible target directions. Let us denote the efficiency of the detector in the ith quadrant by ϵ_{ik} and the luminosity accumulated with a given polarization state by λ_k. The measured yields Y_{ik} then become

$$Y_{ik}=\epsilon_i\cdot(\sigma_{ik})\cdot\lambda_k. \tag{7}$$

If the detector efficiencies are the same in all quadrants, and if the integrated luminosity in all four polarization states is the same, the ratio between any two σ_{ik} is known, and it is easy to see that the quantities $P\cdot A_y$, $Q\cdot A_y$, and $P\cdot Q\cdot A_{mn}$ can be calculated by making use of the known sign with which they appear in the cross section [Eqs. (2)–(4)]. In a real experiment the efficiencies ϵ_i and luminosities λ_k are never exactly the same, even though an effort was made to make them as similar as possible.

As it turns out, there is a method to treat the diagonal matrices ϵ_1 and λ_k in Eq. (7) as unknowns, in addition to the matrix σ_{ik} of interest. This is possible, because we know something about the sums of rows and columns of σ_{ik}/σ_0. For instance, the row sum (over k) is always 4, since all polarization terms cancel. Likewise, it is also clear that the sum (over i) of all the elements in the first two columns ($k=1,2$) equals the sum of the last two columns ($k=3,4$). The task is then to find diagonal matrices $(\epsilon_1)^{-1}$ and $(\lambda_k)^{-1}$ in such a way that $(\epsilon_1)^{-1}Y_{ik}(\lambda_k)^{-1}$ results in a matrix with these conditions on the row and column sums. This problem is known to mathematicians as ''diagonal scaling.'' If none of the matrices involved has negative elements, a solution exists, is unique, and can be found by an iterative algorithm that has been developed for this purpose. A review of the mathematical aspects of this problem and its many applications in transportation, accounting, image conditioning, etc., can be found in Refs. [27,28], and references mentioned therein. It is interesting to note that the so-called ''cross-ratio'' method, which is often used when determining the analyzing power from a measurement with spin up and down with symmetric left and right detectors, is completely equivalent to diagonal scaling (in this case with 2×2 matrices).

Application of diagonal scaling, in our case, yields a value for three ratios of detector efficiencies and values for the relative luminosity with positive and negative beam and target polarizations, respectively. Together with the overall normalization of the yield matrix this uses up 6 of the 16 experimentally determined yields Y_{ik}. The remaining 10 numbers determine the ''scaled'' matrix σ_{ik}/σ_0. It can be demonstrated easily that individual terms contributing to σ_{ik} can be collected by choosing an appropriate array of signs, ρ_{ik} with elements +1 or −1 [an example is given in Eq. (5)] and then summing over all elements $\rho_{ik}\cdot\sigma_{ik}$ ($i,k=1,\ldots,4$). Not surprisingly, there are exactly 10 nontrivial different ways to choose an array ρ_{ik}.

At this stage, for each scattering angle bin $\Delta\theta$, there are 30 experimental quantities resulting from the complete measurement with all three target polarization directions. Six of these yield $P_y\cdot A_y$, $Q_x\cdot A_y$, $Q_y\cdot A_y$, $P_y\cdot(Q_x+Q_y)\cdot A_{xx}$, $P_y\cdot(Q_x\cdot Q_y)\cdot A_{yy}$, and $P_y\cdot Q_y\cdot A_{xz}$. Using a calibration for A_y at one angle (see Sec. VIII D), the analyzing power and the spin correlation parameters reported here follow.

The remaining 22 quantities were used to deduce information on the departure of our experiment from an ''ideal'' measurement. For instance, it is possible that the polarization vector of beam or target did not end up exactly in the direction of the coordinate axes. This could result in small ''unwanted'' components of beam or target polarization (see Table I). Furthermore, when a polarization is reversed it is possible that the magnitude or direction is slightly different. The latter results in additional ''nonflipping'' components that are unaffected by a polarization reversal. In the present analysis these spurious polarization components are taken into account to first order. Terms that contain the product of two small components are negligible and are thus omitted.

The analysis method described here has been compared numerically to the alternative method of deducing the observables from a nonlinear least-squares fit where the ingredients in a theoretical expression for the yields are varied to fit the measured yields Y_{ik}. The two methods have been shown to agree. The advantage of the diagonal scaling method lies in its transparency and in the fact that it provides a framework in which the importance of suspected systematic effects can be studied.

C. Corrections

The experiment was designed such that the azimuthal acceptance was centered at the four angles ϕ_i

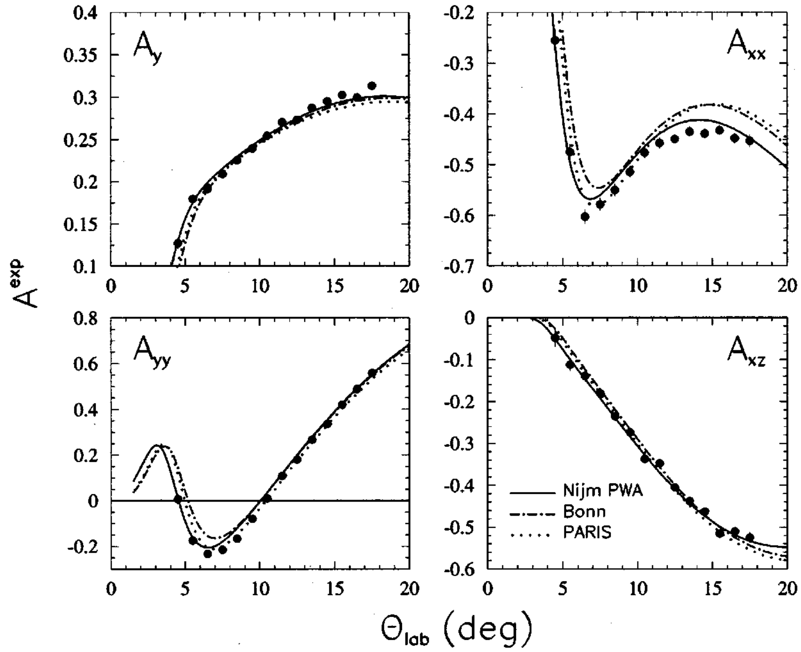

FIG. 13. A_y and A_{mn} vs angle, compared to pp calculations. References for the calculated curves are found in Table IV.

$=(45°,-45°,-135°,135°)$ and the analysis method assumes that this is exactly true. At the larger scattering angles, however, the uneven outer rim of the forward detector system caused a slight nonuniformity of the azimuthal acceptance. The departure of the actual centroid azimuth from the canonical values was determined by averaging the measured ϕ, event by event. The effect of this centroid shift on the data was estimated using simulated yields, and a correction was applied to the data (the change of any A_{mn} was always less than 0.001).

For a given angle bin, 1° wide, the measured A_{mn} is weighted according to the angular dependence of the cross section within that angle bin, and the measurement is not at the exact center of the bin. Our final values for A_{mn} are quoted for the bin center. The applied corrections were of the order of 0.002 and were calculated from the observables as predicted by a VPI phase shift analysis (solution C200 [29]).

D. Absolute normalization

The experiment determines three separate relative angular distributions of the analyzing power, namely, $P_yA_y(\theta)$, $Q_xA_y(\theta)$, and $Q_yA_y(\theta)$. These were combined into a single relative angular distribution $kA_y(\theta)$ by renormalizing two of them to the third such as to minimize the rms deviation between them and then forming the weighted mean of the three values at each angle.

As a next step, the scale factor k was determined by drawing a smooth curve through $kA_y(\theta)$ and matching the curve at one particular angle ($\theta_{\rm lab}=8.64°$) to an absolute calibration point. The smooth curve was obtained from a sixth-order polynomial expansion of $kA_y(\theta)$ about 8.64° whose

TABLE II. Analyzing power A_y and spin correlation coefficients A_{mn}. In addition to the statistical uncertainties shown, the results are subject to a scale factor uncertainty of $\pm1.3\%$ for A_y and $\pm2.4\%$ for A_{mn}.

$\theta_{\rm lab}$ (deg)	A_y	A_{xx}	A_{yy}	A_{xz}
4.5	0.1273 ± 0.0062	-0.2552 ± 0.0216	0.0069 ± 0.0216	-0.0483 ± 0.0210
5.5	0.1797 ± 0.0046	0.4745 ± 0.0152	-0.1740 ± 0.0150	-0.1120 ± 0.0145
6.5	0.1916 ± 0.0040	-0.6026 ± 0.0138	-0.2326 ± 0.0136	-0.1395 ± 0.0130
7.5	0.2092 ± 0.0036	-0.5781 ± 0.0127	-0.2152 ± 0.0125	-0.1806 ± 0.0120
8.5	0.2256 ± 0.0034	-0.5499 ± 0.0118	-0.1661 ± 0.0116	-0.2356 ± 0.0112
9.5	0.2397 ± 0.0032	-0.5138 ± 0.0111	-0.0792 ± 0.0108	-0.2734 ± 0.0105
10.5	0.2545 ± 0.0030	-0.4763 ± 0.0105	0.0100 ± 0.0103	-0.3376 ± 0.0101
11.5	0.2707 ± 0.0029	-0.4572 ± 0.0100	0.1087 ± 0.0098	-0.3483 ± 0.0097
12.5	0.2736 ± 0.0028	-0.4493 ± 0.0097	0.1798 ± 0.0095	-0.4054 ± 0.0094
13.5	0.2872 ± 0.0027	-0.4348 ± 0.0094	0.2673 ± 0.0093	-0.4375 ± 0.0091
14.5	0.2953 ± 0.0026	-0.4383 ± 0.0092	0.3361 ± 0.0091	-0.4635 ± 0.0089
15.5	0.3027 ± 0.0026	-0.4319 ± 0.0091	0.4202 ± 0.0091	-0.5152 ± 0.0089
16.5	0.2999 ± 0.0027	-0.4481 ± 0.0097	0.4887 ± 0.0097	-0.5104 ± 0.0094
17.5	0.3134 ± 0.0038	-0.4530 ± 0.0132	0.5596 ± 0.0133	-0.5251 ± 0.0128

coefficients were adjusted for best fit to the data. The relative uncertainty of the interpolated value at 8.64° is found to be 0.94%. Had a fifth-order or a seventh-order polynomial been used instead, the value at 8.64° would have remained the same, but the quality of fit (χ^2) would have been slightly worse.

An absolute measurement of the pp analyzing power is available at a nearby energy (183.1 MeV), which has an accuracy of 0.80% [A_y(8.64°, 183.1 MeV)$=0.2122\pm0.0017$; see Ref. [24]]. This value was extrapolated to the present energy by comparing the ratio [A_y(8.64°, 197.8 MeV)]/[A_y(8.64°, 183.1 MeV)] for different pp potential models and for different pp partial-wave analyses. The references to the calculations are listed in Table IV. While different theories differ significantly in the predicted values of A_y, the ratios between the values of A_y at the two energies are nearly model independent. The mean value of the ratio is $R=1.0804\pm0.0039$. Adding this 0.36% uncertainty to the uncertainty of the primary calibration point yields our secondary calibration point

$$A_y(8.64°,197.8\ \text{MeV})=0.2293\pm0.0020. \tag{8}$$

If we take into account in addition the 0.94% uncertainty of the interpolated measurements at 8.64°, the overall rms calibration uncertainty in the determination of A_y is $\pm1.3\%$. Figure 13 and Table II show the resulting values of $A_y(\theta)$ with their statistical errors.

The known $A_y(\theta)$ were used to determine the weighted means of P_y, Q_x, and Q_y from the measured values of $P_yA_y(\theta)$, $Q_xA_y(\theta)$, and $Q_yA_y(\theta)$. Since Q_x and Q_y were consistent (see Table I), the target polarization for all three guide fields was assumed to be given by the arithmetic mean of the two values.

The scale factor uncertainties for the A_{mn} were calculated from the scale uncertainty of $P\cdot Q$, taking into account error correlations. Since the uncertainty of the calibration point Eq. (8) of A_y enters twice, once for P and once for Q, the normalization error is larger for the A_{mn} than for A_y. The values of the A_{mn} in Table II have a scale factor uncertainty of $\pm2.4\%$.

The statistical error for each entry in Table II was calculated directly from the uncertainty of the raw yields, by varying the number of counts one by one and calculating the change in the final result as the rms value of the individual changes.

IX. SYSTEMATIC ERRORS

A. Background

Even with the thin-walled target cell used here, the mass of the wall is about 10^9 times larger than the mass of the polarized H target itself, so that one has to address the possibility of background caused by interaction of beam halo with the cell walls or with other material near the target. The requirement that a forward track be in coincidence with a recoil detector in the opposite quadrant suppresses the background to a large extent. However, quasifree scattering of protons from the cell walls, which contain C and F, may in some cases be indistinguishable from free pp scattering in the target gas. It thus seemed important to carry out a number of tests to place an upper limit on background.

(a) ^{4}He target: removal of the H target gas reduces beam heating and thus affects the properties of the circulating beam. In this test, beam heating was provided by admitting He to the target cell. The resulting distribution of events is compared to the events with H in the left two frames of Fig. 14. Using the same analysis for the He target as for the H target but excluding events near the He locus, one finds (normalized to 1 C of charge passing through the target) 62 000 events for the polarized H target compared to 396 pp-like events for the He target. The corresponding background rate of 0.6% is presumably an upper limit, because some of the background seen with He could in fact be caused by residual H in the target or by $(p,2p)$ reactions on He.

(b) Empty target: beam heating was introduced by a N_2 jet target in another straight section of the ring. The corresponding spectra (right-hand side of Fig. 14) clearly show traces of residual gas; i.e., most background events appear to be caused by *p-p* or *p*-He scattering, depending on what gas was previously used as target. In addition, the analyzing power for the pp-like events agrees within statistics with that

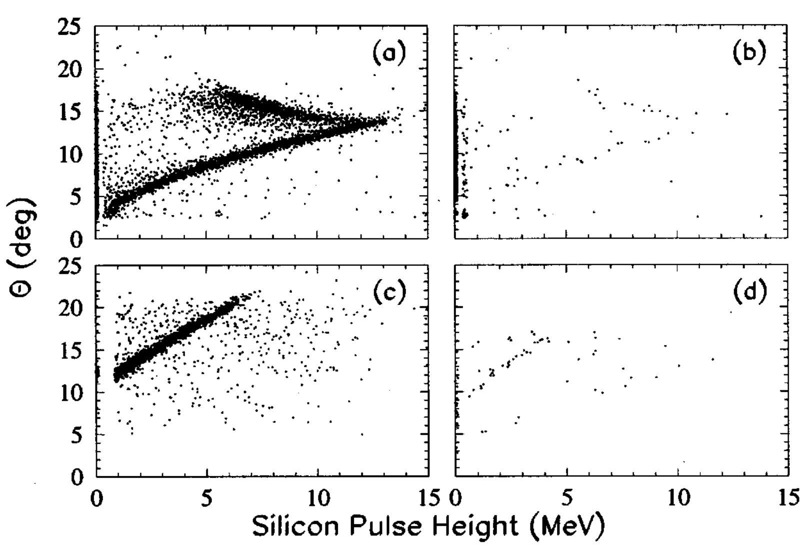

FIG. 14. Forward-scattering angle θ vs recoil energy for H target (a) and He target (c). Corresponding empty-target runs are shown on the right (b), (d). For the empty target runs, a N_2 target in another straight section of the ring provided beam heating. The background run for He was separated in time from the He run by four other empty-target runs. In both empty-target runs, residual gas from previous He and H runs is clearly visible.

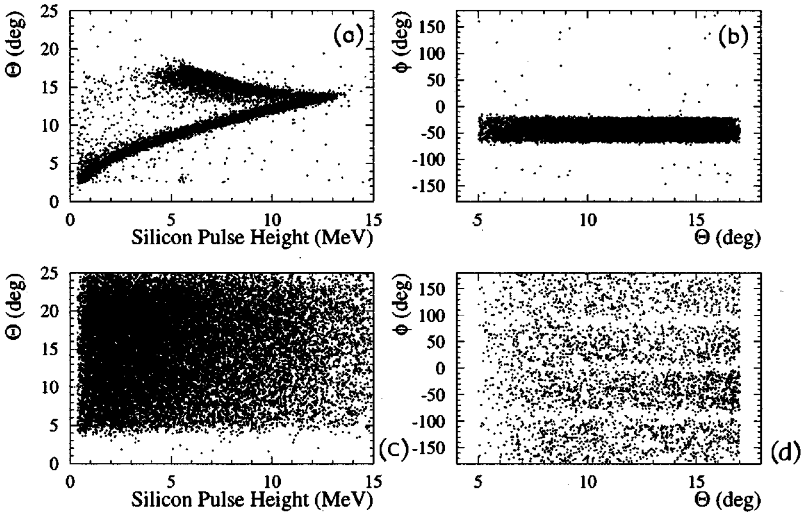

FIG. 15. Comparison of runs with H target [pp events, frames (a) and (b)] and N_2 target [background events, frames (c) and (d)]. All events shown are coincident events associated with one particular recoil detector ($\phi = -45° \pm 18°$). On the left, forward angle θ vs recoil pulse height, on the right ϕ vs θ.

of free pp scattering. The fraction of pp-like events with empty target compared to pp events with polarized H target is 1.0% for background runs following H runs. These events have the same analyzing powers as good pp events and are thought to be caused primarily by residual gas rather than background.

(c) Noncoplanarity: even tighter limits on background can be obtained by noting that the forward and recoil particles from background events, such as (p,px) reactions on C or F in the cell walls, are in general not coplanar, contrary to free pp scattering. To study the characteristics of background events, N_2 gas was admitted to the target cell, on the assumption that the incident proton energy (200 MeV) is high enough that the specific nuclear structure of the nucleus producing the background is not important. For the measurements with the polarized H target (top two frames of Fig. 15), potential background events are events which are outside the pp locus in the left-hand graph or outside the proper ϕ range (''noncoplanar event'') in the right-hand graph. The fraction of noncoplanar to coplanar events is 0.0039 for the H target and 1.2 for the N_2 target. If we assume that the background events with H in the target have the same characteristics as the events observed with N_2, the fraction of coplanar background events for H is thus 0.3%. However, about 1/3 of these events are rejected by the condition that good events must have the correct recoil energy for a given scattering angle.

A conservative final estimate for background is (0.2 ± 0.2)%.

TABLE III. Amplitudes of beam position and beam angle changes caused by reversal of the guide field over the target.

	X-guide field	Y-guide field	Z-guide field
Position modulation in μm			
x	-7 ± 4	-22 ± 4	-4 ± 4
y	11 ± 4	-1 ± 4	-5 ± 5
Angle modulation in μrad			
x tilt	20 ± 49	31 ± 49	-35 ± 49
y tilt	101 ± 49	-21 ± 49	-9 ± 49

B. Beam motion associated with guide field reversal

Even though the guide field over the target is weak (Sec. II D), changes in beam position and beam angle associated with reversal of the guide field must be considered, since they can cause small changes in count rates that contaminate the polarization-dependent changes in count rates. Angle modulation associated with guide field reversal (i.e., target polarization reversal), for instance, would cause a modulation in scattering angle and thus a modulation in count rate that is indistinguishable from an asymmetry caused by a target analyzing power. Thus, one way that modulations in beam angle and beam position would manifest themselves would be to cause an apparent target polarization for unpolarized H_2 in the target cell. That these effects are small is shown by the absence of spurious target polarization in runs with unpolarized H_2 (see Table I). However, closer limits on beam modulations and their effects on the spin correlation parameters were determined as follows: Section IV showed how the beam position relative to the wire chambers was determined from the forward track and the recoil detector signal. The same methods were used to study beam motion associated with guide field reversal, by sorting the data according to guide field currents. Values for the amplitude of position and angle modulations are listed in Table III.

The effects of these beam modulations on the measured spin correlation parameters were estimated by Monte Carlo calculations, which produced simulated yields as a function of θ for all four quadrants in ϕ. These simulated yields changed as the beam position or angle was changed. We then forced the same changes on the actual data yields in the appropriate spin states. By analyzing these modified yields, we could deduce the effect on the A_{mn} results. Since the effects were quite small, beam position modulations of 0.5 mm, 1.0 mm, and 2.0 mm and angle modulations of 0.1 ° (1.75 mrad) were simulated. The effects of position changes were found to be proportional to the displacement, as expected. For the beam displacements given in Table III, the maximum change in any A_{mn} scales to 1.3×10^{-4} and is therefore neglected. Similarly, the maximum change in any A_{mn} due to the 0.1° angle modulation was found to be 0.0015. Scaling this to the 0.15 mrad maximum modulation from Table III gives an effect of the same negligible magnitude.

TABLE IV. Comparison between the data of Table II and different partial-wave and potential-model analyses. An overall scale factor κ for A_y and κ^2 for A_{mn} was allowed. The χ^2 summed over the 14 data points of the angular distribution is given for each observable. Also given is the sum of the χ^2 for all observables and the overall χ^2 per degree of freedom.

	Type of analysis	Ref.	κ	χ^2 (14 angles) A_y	A_{xx}	A_{yy}	A_{xz}	Sum	χ^2/N_{DOF}
C200		[29]	0.9902	27.7	17.0	6.9	23.1	74.7	1.36
SM94	Partial	[7]	0.9887	52.4	52.5	29.9	52.1	186.9	3.40
VZ40	wave	[7]	0.9978	38.3	206.0	136.8	42.1	423.2	7.69
FA95	analysis	[30]	0.9906	41.7	50.7	61.3	41.0	194.8	3.54
VV40		[30]	0.9954	38.4	52.4	44.0	22.4	157.2	2.86
NJM PWA		[31]	0.9933	34.9	28.6	63.9	24.4	151.8	2.76
Paris		[32]	0.9957	99.1	178.7	115.9	114.1	508.7	9.25
Bonn		[33]	0.9945	57.4	199.9	385.8	57.6	700.7	12.74
CD-Bonn		[34]	0.9880	40.8	20.9	11.7	21.7	95.1	1.73
NJM93	Potential	[35]	1.0091	120.1	17.0	96.1	54.2	287.4	5.23
NJM I	models	[35]	0.9909	39.4	13.3	16.5	13.9	83.1	1.51
NJM II		[35]	0.9906	43.3	15.9	33.2	17.4	109.8	2.00
AV18		[36]	0.9895	63.7	46.0	72.5	22.7	204.9	3.73
Reid93		[35]	0.9929	34.5	30.4	40.7	20.5	126.1	2.29

C. Other systematic errors

As stated in Sec. IV above, the average beam position was seen to change during the course of this experiment, but the actual position was determined for every run and accounted for in the calculation of scattering angles and A_{mn}'s. However, the uncertainty in this position, estimated at ± 0.1-mm, could also be a source of systematic error. This effect was evaluated by the same Monte Carlo method described above, except that the beam displacements were not synchronized with polarization reversals. The result of a 0.1-mm error in the transverse beam position was found to be less than 5×10^{-4} in any A_{mn}. Similarly, the $\pm 0.05°$ uncertainty in the absolute beam angle corresponds to a change of at most 8×10^{-4} in any A_{mn}. Both of these systematic errors are negligible compared to the normalization uncertainty.

Computer dead time causes a systematic error if the trigger rate depends on beam or target spin orientation. A significant change in count rate ($\pm 6\%$) was observed when Q_y was reversed, as expected since the total cross section for parallel and antiparallel target and beam spin differs. The number of pulses lost was determined by comparing the trigger rate read on a scaler to the number of events processed by the computer. The average change in dead time when Q_y is reversed was found to be 0.2%. The dead-time correction is nearly angle independent and changed the values of A_{xx} and A_{yy} by 0.002.

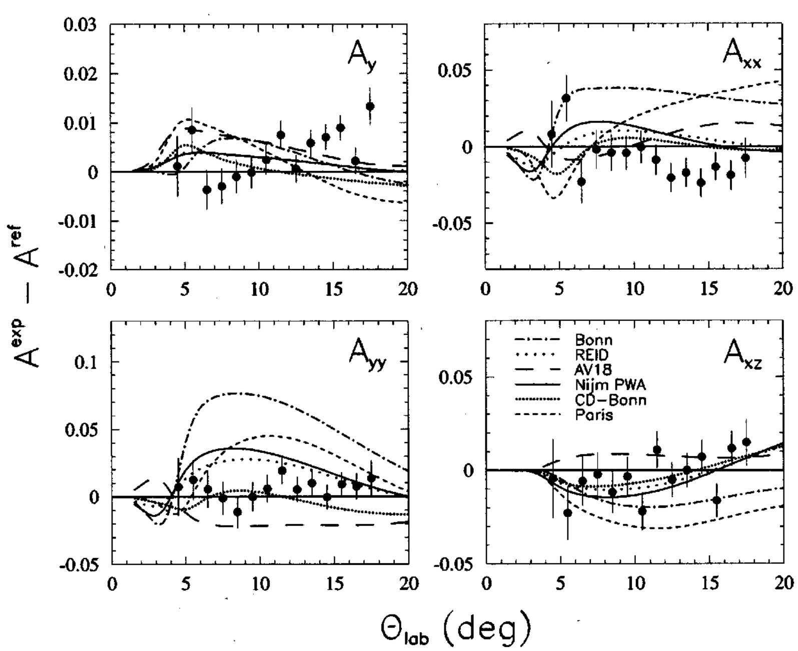

FIG. 16. Comparison between data and different models of the pp interaction. In order to display small differences more clearly, reference values A^{ref}, calculated from the C200 phase shift solution [see Ref. [29]), are subtracted. For other references to the calculated curves, see Table IV.

Other systematic error sources which were considered showed negligible effects. The magnetic guide field over the target cell as well as the ambient external field changes along the cell, so that the direction of target polarization may have a small dependence on z. The effect on the measured A_{mn} is less than 2×10^{-3} and was neglected. The actual measured orientations of the average target and beam polarizations with respect to the desired directions are taken into account in the analysis.

X. COMPARISON TO THEORY

In this section we compare the new results to predictions based on pp partial-wave analyses and on pp potential models. While a large number of pp calculations exist in the literature, here we limit ourselves to papers published during the last three years. An exception is made for pp potential model calculations, where we also compare to the most frequently cited earlier potentials, such as the Paris potential and the Bonn potential, which have been important in nuclear structure or three-body calculations.

Since many of the calculations give quite similar results, the small differences can be displayed more clearly by subtracting reference values $A^{\mathrm{ref}}(\theta)$. The choice of this reference is arbitrary and irrelevant to the conclusions. Here, we choose as reference a partial-wave analysis by the VPI group [29] called C200, which is simply a phenomenological fit to all previous pp data between 175 MeV and 225 MeV. The C200 solution imposes a requirement of continuity of phase shifts with neighboring energy intervals, but other than that is relatively devoid of theoretical input.

In comparing the present measurements with calculations, we take into account that the measurements have an overall normalization uncertainty. Thus in each case, the measurements were scaled by normalization factors κ and κ^2 for A_y and A_{mn}, respectively, until best agreement with the calculation is reached. The scale factor for the A_{mn} is the square of the scale factor for A_y because the A_{mn} involve beam and target polarization. Table IV lists the values of κ and the quality of agreement (χ^2) between measurements and calculations for different theories. In all cases, the required κ is compatible with the normalization error discussed in Sec. VIII D.

Among the partial-wave analyses, best agreement is found for the C200 solution mentioned above. Of the analyses which are based on all pp and np data and which cover a wide range of energies, the Nijmegen partial-wave analysis (0–350 MeV) is of particular interest because it gives an excellent representation of the pp and np data over this energy range, with a χ^2/N_{DOF} of 1.08 [31]. The analysis assumes that charge independence is broken. The agreement with the present results is good, except that A_{yy} deviates significantly from the measurements (see also Fig. 16). Of the many analyses published by the VPI group, Table IV lists four recent calculations. Solution SM94 is a VPI energy-dependent partial-wave analysis of np and pp data for the range 1–1600 MeV. The updated version of the same analysis (FA95) gives the same quality of fit. However, for the more limited energy range of 1–400 MeV, the new version (VV40) is much improved over the previous one (VZ40).

The potential models listed in Table IV include the widely used Paris potential [32] and the Bonn full model potential [33]. Neither represents the new data very well. Better agreement is found for the updated Nijmegen soft-core potential NJM93 [35] which is a conventional meson-exchange potential. However, based on our limited data, we confirm the conclusion that none of the conventional meson-exchange potentials can compete in quality with the Nijmegen partial-wave analysis. The Nijm I and Nijm II potentials are attempts to improve the agreement with data by slightly adjusting the potential for each particular partial wave. For our data, these adjusted potentials give much better agreement, in the case of Nijm I nearly equal to the best partial-wave analysis. A similar, excellent fit is obtained with the new CD-Bonn potential [34]. This potential is based on the Bonn full potential [33], but small adjustments were allowed in each partial wave for the parameters that govern the correlated multiple-pion exchange. The calculation labeled AV18 refers to the Argonne potential [36], with charge independence breaking. This potential has been fit directly to the Nijmegen pp and np scattering parameters and the deuteron binding energy in the energy range 0–350 MeV. While this potential gives a good fit to all previous np and pp data ($\chi^2/N_{\mathrm{DOF}}=1.08$), it does not agree well with the present values of A_{yy} (Fig. 16). The Reid potential (RID93, Table IV) discussed in the recent Nijmegen paper [35] is an updated Reid-like potential, based on the original Reid potential of 1968. The excellent agreement with our data (see also Fig. 16) is consistent with the remark in Ref. [35] that this potential provides as good a fit to the pp data set as the Nijmegen partial-wave analysis.

The most noteworthy conclusion of these comparisons is that our limited data set at one energy very closely mirrors the agreement or disagreement of the different theories with the world data set of all types of NN data.

XI. CONCLUSIONS

A polarized hydrogen target was formed by injecting polarized atoms into a T-shaped cell with an aperture of 8 mm $\times$ 8 mm through which the circulating polarized beam of the IUCF proton storage ring (Cooler) passed. Elastic scattering events in the angular range 4.5°–17.5° could be detected free of background by recording coincidences between forward-scattered protons and recoils. One of the great advantages of this method compared to the use of conventional solid targets containing polarized H is the lack of target contaminants and the ease with which the target atoms can be manipulated in sign and direction of polarization on a time scale of seconds rather than hours. Thus A_y and the spin correlation parameters A_{xx}, A_{yy}, and A_{xz} could be measured at the same time. In addition, the absence of large magnets near the target permitted measurements at all angles at the same time. In spite of the small target thickness viewed by the detectors (2.2×10^{13} polarized H/cm^2), the data presented here were accumulated in 1 week, including beam tuning and overhead. No deterioration of target polarization was observed over this time period. The circulating beam intensity and thus the event rate were improved by storing the circulating beam for about 2 h, and replenishing the intensity by periodically injecting additional beam. The sign of polarization of the stored beam was flipped periodically with suitable rf fields (spin flipper). We conclude that precision measurements of the spin dependence even at forward angles can be made, essentially free of background, with this technique.

For absolute calibration, the present measurements of spin correlation parameters A_{mn}, and analyzing power A_y at 197.8 MeV, made use of a previous, accurate analyzing power measurement at a nearby energy (183.1 MeV). The measurements were compared to different pp partial-wave analyses and a number of NN potential models. These parametrizations are typically based on a few thousand observations of pp and np scattering over a wide range of energies, usually 0–350 MeV or 0–1.6 GeV. We find fair agreement with those calculations that give a good fit to the global data set and poor agreement with those that do not. However, inclusion of the new data in these global analyses should lead to some refinement of the phase shifts since the database previously contained no accurate spin correlation data between 100 MeV and 300 MeV.

In view of the successful completion of this experiment, the measurements are being extended in angle all the way to $\theta_{\mathrm{c.m.}} = 90°$ and in energy from the present energy to 450 MeV. In addition, spin precessors are being readied to permit not only the transverse beam polarization used here, but also longitudinal beam polarization. Completion of this next stage of experiments is expected to provide a significant enhancement of the pp database. The new polarized beam and target capabilities will pave the way for studies of spin-spin effects in pion production.

ACKNOWLEDGMENTS

We thank Dr. M. Rentmeester and Dr. R. Machleidt for providing tables of spin correlation coefficients for the Nijmegen and Bonn Potentials, respectively. We are grateful for the untiring efforts of the accelerator operations group at IUCF, in particular D. Friesel and T. Sloan. This work was supported in part by the National Science Foundation and the Department of Energy. One of us (F.R.) would also like to thank the Alexander von Humboldt Foundation for their generous support.

[1] V. F. Dmitriev, D. M. Nikolenko, S. G. Popov, I. A. Rachek, Yu. M. Shatunov, D. K. Toporkov, E. P. Tsentalovich, Yu. G. Ukraintsev, B. B. Voitsekhovskii, and V. G. Zelenski, Phys. Lett. **157B**, 143 (1985).

[2] R. Gilman, R. J. Holt, E. R. Kinney, R. S. Kowalczyk, S. I. Mishnev, J. Napolitano, D. M. Nikolenko, S. G. Popov, D. H. Potterveld, I. A. Rachek, A. B. Temnykh, D. K. Toporkov, E. P. Tsentalovich, B. B. Wojtsekowski, and L. Young, Phys. Rev. Lett. **65**, 1733 (1990).

[3] M. A. Miller *et al.*, Phys. Rev. Lett. **74**, 502 (1995); C. Bloch *et al.*, Nucl. Instrum. Methods Phys. Res. A **354**, 437 (1994).

[4] K. Zapfe, B. Braun, H.-G. Gaul, M. Grieser, B. Povh, M. Rall, E. Steffens, F. Stock, J. Tonäuser, C. Montag, F. Rathmann, D. Fick, and W. Haeberli, Rev. Sci. Instrum. **66**, 28 (1995).

[5] W. Haeberli, in *Nuclear Physics with Stored, Cooled Beams*, edited by P. Schwandt and H. O. Meyer, AIP Conf. Proc. No. 128 (AIP, New York, 1984); S. S. Hanna, in *Proceedings of the 4th International Symposium on Polarization Phenomena in Nuclear Reactions*, Zürich, 1975 [Exp. Suppl. (Birkhäuser) **25**, p. 407 (1976)].

[6] J. R. Bergervoet, P. C. van Campen, R. A. M. Klomp, J. L. de Kok, T. A. Rijken, V. G. J. Stoks, and J. J. de Swart, Phys. Rev. C **41**, 1435 (1990).

[7] R. A. Arndt, I. I. Strakovsky, and R. L. Workman, Phys. Rev. C **50**, 2731 (1994).

[8] M. M. Gazzaly, G. Pauletta, N. Tanaka, B. Aas, H. Fujisawa, S. Greene, H. Hasai, S. Isagawa, G. Igo, S. Ishimoto, K. Jones, D. Lupiano, A. Masaike, J. McClelland, C. L. Morris, F. Nishyama, Y. Ohashi, A. Ohashi, L. Santi, F. Sperisen, G. Weston, and C. Whitten, Phys. Rev. Lett. **58**, 1084 (1987).

[9] B. von Przewoski *et al.*, Bull. Am. Phys. Soc. **40**, 1629 (1995).

[10] T. Wise, A. D. Roberts, and W. Haeberli, Nucl. Instrum. Methods Phys. Res. A **336**, 410 (1993).

[11] W. Haeberli, Annu. Rev. Nucl. Sci. **17**, 373 (1967).

[12] J. S. Price and W. Haeberli, Nucl. Instrum. Methods Phys. Res. A **349**, 321 (1994).

[13] R. E. Pollock, V. Derenchuk, X. Pei, T. Sloan, F. Sperisen, H. O. Meyer, B. v. Przewoski, T. Rinckel, P. Pancella, M. A. Ross, and W. K. Pitts, Nucl. Instrum. Methods Phys. Res. A **330**, 380 (1993).

[14] M. A. Ross, W. K. Pitts, W. Haeberli, H. O. Meyer, S. F. Pate, R. E. Pollock, B. v. Przewoski, T. Rinckel, J. Sowinski, F. Sperisen, and P. V. Pancella, Nucl. Instrum. Methods Phys. Res. A **326**, 424 (1993).

[15] W. Haeberli, *Proceedings of the 9th International Symposium on High Energy Spin Physics*, Bonn, 1990 (Springer, Berlin, 1991), Vol. 2, p. 194.

[16] M. A. Ross, A. D. Roberts, T. Wise, W. Haeberli, W. A. Dezarn, J. Doskow, H. O. Meyer, R. E. Pollock, B. von Przewoski, T. Rinckel, F. Sperisen, and P. V. Pancella, Nucl. Instrum. Methods Phys. Res. A **344**, 307 (1994).

[17] W. R. Lozowski, J. Hudson, and W. A. Dezarn, Nucl. Instrum. Methods Phys. Res. A **362**, 189 (1995).

[18] Type J Silicon Strip detectors, supplied by Micron Semiconductor Ltd., Lancing, Sussex, England.

[19] K. Solberg, A. Eads, J. Goodwin, P. Pancella, H. O. Meyer, and T. Rinckel, Nucl. Instrum. Methods Phys. Res. A **281**, 283 (1989).

[20] H. O. Meyer, C. Horowitz, H. Nann, P. V. Pancella, S. F. Pate, R. E. Pollock, B. von Przewoski, T. Rinckel, M. A. Ross, and F. Sperisen, Nucl. Phys. **A539**, 633 (1992).

[21] V. Derenchuk, A. Belov, R. Brown, J. Collins, J. Sowinski, E. Stephenson, and M. Wedekind, in *Polarization Phenomena in Nuclear Physics*, edited by E. Stephenson and S. Vigdor, AIP Conf. Proc. No. 339 (AIP, New York, 1995), p. 662.

[22] D. D. Caussyn *et al.*, Phys. Rev. Lett. **73**, 2857 (1994).

[23] B. von Przewoski, W. A. Dezarn, J. Doskow, J. G. Hardie, H. O. Meyer, R. E. Pollock, T. Rinckel, F. Sperisen, W. Haeberli, B. Lorentz, F. Rathmann, T. Wise, and P. V. Pancella, Rev. Sci. Instrum. **67**, 165 (1996).

[24] B. von Przewoski, H. O. Meyer, P. V. Pancella, S. F. Pate, R. E. Pollock, T. Rinckel, F. Sperisen, J. Sowinski, W. Haeberli,

W. K. Pitts, and J. S. Price, Phys. Rev. C **44**, 44 (1991).

[25] H. O. Meyer, Phys. Rev. E **50**, 1485 (1994).

[26] F. Rathmann, C. Montag, D. Fick, J. Tonhäuser, W. Brückner, H.-G. Gaul, M. Grieser, B. Povh, M. Rall, E. Steffens, F. Stock, Kirsten Zapfe, B. Braun, G. Graw, and W. Haeberli, Phys. Rev. Lett. **71**, 1379 (1993).

[27] A. W. Marschall and I. Olkin, Numer. Math. **12**, 83 (1968).

[28] U.G. Rothblum and H. Schneider, *Linear Algebra and its Applications* (Elsevier, New York, 1989).

[29] R.A. Arndt *et al.*, solution of C200 of the VPI SAID program, accessed by TELNET 128.173.176.61. Login as PHYSICS, password QUANTUM.

[30] R. A. Arndt, *et al.*, update of solutions SM94 and VZ40; see Ref. [29].

[31] V. J. G. Stoks, R. A. M. Klomp, M. C. M. Rentmeester, and J. J. deSwart, Phys. Rev. C **48**, 7921 (1993).

[32] M. Lacombe, B. Loiseau, J. M. Richard, R. Vin Mau, J. Côté, P. Pirés, and R. de Tourrreil, Phys. Rev. C **21**, 861 (1989).

[33] R. Machleidt, K. Holinde, and Ch. Elster, Phys. Rep. **149**, 1 (1987); R. Machleidt and G. Q. Li, *ibid.* **242**, 5 (1994).

[34] R. Machleidt, F. Sammarruca, and Y. Song, Phys. Rev. **53**, 1483 (1996); R. Machleidt (private communication).

[35] V. J. G. Stoks, R. A. M. Klomp, C. P. F. Terheggen, and J. J. deSwart, Phys. Rev. C **49**, 2950 (1994).

[36] R. B. Wiringa, V. G. J. Stoks, and R. Schiavilla, Phys. Rev. C **51**, 38 (1995).